Hindawi
Advances in Civil Engineering
Volume 2022, Article ID 7827506, 15 pages
https://doi.org/10.1155/2022/7827506

Research Article

Seismic Performance and Mechanical Mechanism of Steel-Enhanced Damping Concrete Core Wall with Concealed Steel Plate Bracings under Oblique Loading

Zhangqi Hu,[1] **Taohua Chen**,[2] **Mengfu Wang**,[3] **Weirong Lu**,[4] **and Ran He**[1]

[1]*College of Civil Engineering, Hunan City University, Yiyang 413000, China*
[2]*Yiyang Central Hospital, Yiyang 413000, China*
[3]*College of Civil Engineering, Hunan University, Changsha 410082, China*
[4]*College of Civil Engineering, Hunan University of Science and Technology, Xiangtan 411201, China*

Correspondence should be addressed to Zhangqi Hu; huzhangqi0413@163.com

Received 28 January 2022; Revised 13 April 2022; Accepted 28 April 2022; Published 1 June 2022

Academic Editor: Yiwei Weng

This article focuses on the seismic performance and mechanical mechanisms of core walls under biaxial earthquakes. Through the oblique loading test (biaxial loading test) on one 1/6 scale steel-enhanced damping concrete core wall with steel plate bracings, the failure patterns, the load-bearing capacities, the yield mechanisms, and the strain distributions, etc. were investigated. Comparisons were made with the available test results of the authors' previously unidirectional tested core walls and the tests completed by other scholars. The oblique tested core walls exhibited lower initial stiffness, but higher yield displacements, loading capacities, and ultimate displacements. A much more serious damage was also found in the wall limbs of oblique tested core walls by comparing with the unidirectional test core walls. Then finite element analysis (FEA) was also carried out to study the axial compression ratio (n), coupling beam span-depth ratio (l/h) on the stress distributions, and effective width of the end wall limbs (b_e). From the analysis results, it can be indicated that l/h affects much the stress distributions of oblique test core wall, which would be in eccentric force states if the coupling beam span-depth ratio was small, while the axial compression ratio does not affect the stress distributions dramatically. b_e varies with loading steps, the minimum value ($b_{e,\,\min}$) of which increases with the decrease of l/h, and $b_{e,\,\min}$ will grow along with n.

1. Introduction

Reinforced concrete (RC) core walls possess the advantages of high stiffness, high bearing capacity, and flexible space arrangement; thus they have been widely used in high rise buildings. But for economical and antiseismic reasons, RC core walls are not suitable for the over 300 m high buildings (super tall buildings) which are increasingly popular in recent years. The recent earthquake disasters, such as the Chile Maule Earthquake (2010) and New Zealand Christchurch Earthquake (2011), suggested that the seismic performance of RC high rise buildings should be improved. Normally, adding steel to crucial part of core wall to form the steel-concrete composite core wall (SCCW) or improving the concrete performance can significantly enhance the seismic performance of them.

Taking the advantageous characteristics of both the steel and concrete materials, the SCCWs can not only improve their bearing capacity and deformation capacity, but also reduce the wall thickness compared to the traditional RC core walls. Hence, the SCCWs have been growingly used in super tall buildings, and scholars have consequently conducted significant studies on SCCWs as well. For instance, Cao et al. [1] proposed the composite shear wall with rectangular concrete filled steel tube columns (SWSTC), and it was then applied in the Guangzhou Central Business District in the form of core wall (CWSTC). Though SWSTC showed good seismic performance, the steel tube columns

and concrete shear walls were not connected well enough. Thereafter, Dong et al. [2] came up with the composite core wall with steel tube-reinforced concrete columns (CCWSTC), in which the tube-reinforced concrete columns worked well with shear walls, and compared with CWSTC, the CCWSTC had more uniformly and widely distributed cracks and greater energy dissipation capacity, etc. Moreover, much research [3, 4] indicated that applying inclined reinforcements or steel plates in RC wall can significantly improve the seismic performance. Thus, the composite core wall with steel tube-reinforced concrete columns and concealed steel truss (CCWSTCC) was proposed and tested by Zhang et al. [5, 6], and the CCWSTCC exhibited greater bearing capacity and ductility than CCWSTC, but the concealed steel truss should go through the coupling beams, leading to limited coupling beam layout; the coupling beam span-depth ratio of CCWSTCC was only 0.5. Coupling beam is one of the most critical components of shear/core wall. To gain good seismic performance and flexible coupling beam layout, Wang et al. [7] proposed the steel truss reinforced concrete core wall (STRCCW), in which the profile steel was embedded in each column and coupling beam, and RC walls were reinforced with steel trusses (inclined steel plates), an inner frame formed by welding the steel trusses to profile steels. Through quasi-static tests on two specimens, the STRCCW was found to have greater loading capacity and larger equivalent damping ratio than the steel reinforced concrete core wall (SRCCW).

Clearly, the seismic performance of core wall can be importantly influenced by concrete properties, and the damping property is one of them. According to the previous studies [8, 9], the damping property of concrete can be obviously enhanced by introducing the styrene-acrylate emulsion (SAE) [8] or styrene-butadiene rubber (SBR) [9] into the normal concrete, while the compressive strength of concrete decreased significantly. Then the enhanced damping concrete was designed by the authors' team through introducing polypropylene (PP) fibers and both SAE/SBR into normal concrete under proper proportion, which not only ensured good damping performance but also overcame strength reduction [10]. Subsequently, quasi-static tests on steel-enhanced damping concrete composite shear walls with concealed bracings [11, 12] were implemented, whose results indicated that the seismic performance of them in terms of the cracking load, deformation capacity, and energy dissipation capacity was enhanced greatly compared with the steel-normal concrete composite shear wall with concealed bracings.

Our research team [13, 14] then applied the enhanced damping concrete to core wall, and an inner frame was embedded in it, forming the steel-enhanced damping concrete composite core wall with steel plate bracings (SEDCCW). Compared with SRCCW, each coupling beam of SEDCCW was embedded with a steel plate with shear studs instead of profile steel. According to the research by Lam et al. [15, 16], the using of the embedded steel plates has positive effects on enhancing the energy consumption capacity and preventing shear failure in the coupling beams. Through low cyclic reversed loading tests on six 1/6 scale specimen [13], it is indicated that the SEDCCWs have excellent seismic performance.

In seismic design, a core wall can be always divided into several groups of components, in which the coupling beams are the main energy dissipating components, and the webs function as the main shear resistance members, and flanges are the main antiflexural components. Together, these components can provide high rigidity, large loading capacity, and good economic benefits for core walls. However, the division is on the condition that the core walls are subjected to unidirectional loading path, corresponding to the single-dimensional seismic action. When subjected to multi-dimensional earthquakes, the core walls had different division mechanisms, the seismic performance of which can be severely affected [17, 18].

The loading path is one of the key problems to simulate the bidirectional earthquake. Qiu et al. [19, 20] carried out a study on the seismic performance of RC columns under bidirectional loading and compared the influence of different loading paths on the seismic performance of RC columns. Figure 1(a) shows the unidirectional loading path, and Figures 1(b)~1(g) depict six different bidirectional loading paths; from the test results, much more serious damage was found for the bidirectional tested columns by comparing with the unidirectional tested column. Rodrigues et al. [21] completed the bidirectional pseudo-static tests on 24 RC columns and then analyzed and compared the effects of different loading paths on the stiffness degradation, ductility, and bearing capacity of RC columns; Bechtoula [22] and Chang [23] found that, compared with the unidirectional loading test specimen, the stiffness, strength, and ductility of RC columns significantly reduced during bidirectional loading paths, while the cumulative energy consumption increased. According to the research by Song and Li [24], the column hinge failure mechanism would likely be formed when subjected to oblique loads. Niroomandi et al. [25] investigated the effects of bidirectional different loading patterns on the seismic performance of RC shear walls through experimental tests; great increase of strains in concrete and bars was documented, when specimens were subjected to bidirectional loading paths. Some research has been conducted on the multidimensional seismic performance of core walls, for instance: the Japanese nuclear power engineering corporation [26–28] conducted low cyclic reversed loading tests and shaking table tests on circular core walls and square core walls; Du et al. [29] carried out pseudo-static tests on two core walls, one was under the bidirectional loading path shown in Figure 1(b), and the other was the unidirectional test specimen, under the loading path shown in Figure 1(a), and they found that the wall limbs of bidirectional tested core wall were damaged more seriously than unidirectional tested core wall. Hou et al. [30] conducted the diagonal test on one core wall, with the loading path shown in Figure 1(d); the diagonal test core wall was found to have lower initial stiffness, but higher loading capacity compared with unidirectional test core wall, and all wall limbs of them were seriously damaged, while only some horizontal cracks were observed in the flanges of unidirectional tested specimen. In summary, compared with

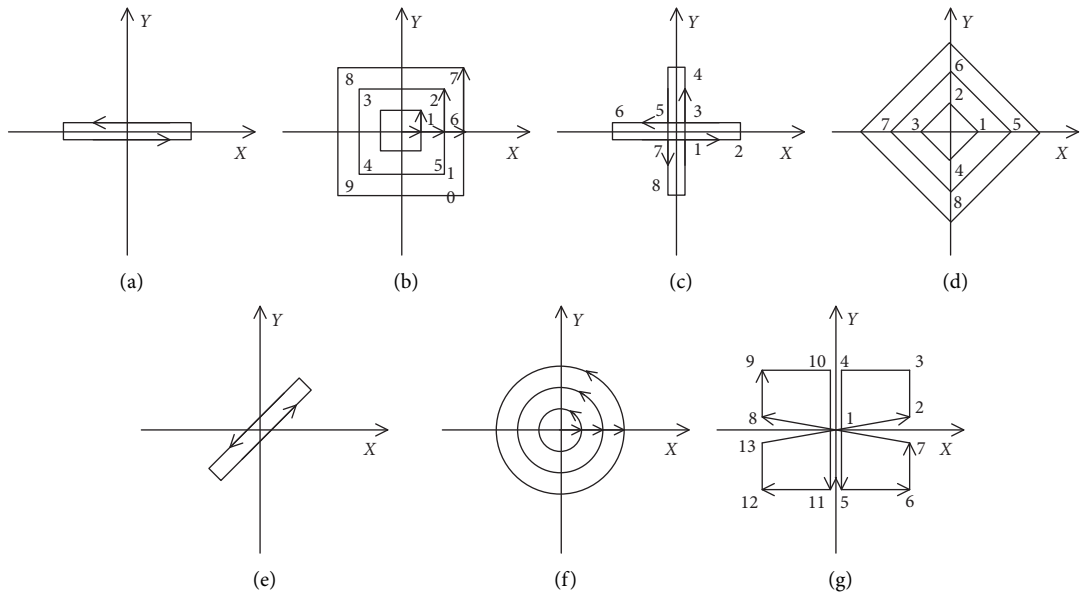

Figure 1: Loading paths [19].

the single-dimensional seismic performance, the internal force distributions and yield mechanisms of structures during multidimensional earthquakes are quite different, and more serious damage was always observed due to the seismic damage overlay from different directions. On the other hand, the research on the multidimensional seismic performance of the core walls is still insufficient; more research needs to be performed, including experiment research and finite element analysis to develop the multidimensional seismic structural design theories for refining the seismic codes. Therefore, it is of great significance to further study the multidimensional structure seismic response of core walls.

Based on our previous research [13, 14], one SEDCCW specimen was designed and diagonally tested in this article and compared with available experimental research to study influence of bidirectional loading paths on the bearing capacity, ductility, strain distribution, failure pattern, etc. of core walls. Finite element analysis (FEA) was also carried out to study the stress distribution characteristics of the core walls with different coupling beam span-depth ratios and axial compression ratios.

2. Experimental Programs

2.1. Specimen Information. On the basis of our previously tested specimen CW4X-1 in [13], one 1/6 scale SEDCCW specimen was designed and tested in this study, denoted as specimen CW4X-D, specimens CW4X-1 and CW4X-D were only varied in loading paths, specimen CW4X-1 was tested with the unidirectional loading path, and the test angle of specimen CW4X-D is 45° (Figure 1(b)). Figure 2 shows the details of SEDCCW: encased steel was embedded in each hidden column and corner column, four layers of steel plate bracings were set in each wall limb, and the coupling beams were reinforced with steel plates, then the steel plate bracings, coupling beam steel plates, and the encased steels were welded together to form an inner frame, and the core wall was casted with the enhanced damping concrete. The main parameters of core wall specimens are shown in Table 1.

2.2. Test Setup and Measuring Scheme. The test setup is shown in Figure 3, in which the specimen was fixed on the rigid floor with high-strength screws, the axial load was applied with hydraulic Jack and remained stable during the test, and the lateral load was applied with a 1000 kN actuator. Concrete strain gauges were plastered on the bottom of wall limbs, and the wall limbs are divided into end wall limbs and middle wall limbs, and the X' axis is the loading direction, which takes a 45° angle with both the X and Y axis (X and Y axis denote the web direction and flange direction, respectively), shown in Figure 4.

2.3. Loading Protocol. Displacement control was employed throughout the test, each loading cycle was repeated twice, the loading protocol is shown in Figure 5, the top drift ratio of core wall θ is equal to Δ/H, where Δ is the top displacement, and H denotes the specimen height, and in this research, it can be taken as $H = 2660$ mm.

3. Test Results and Discussion

3.1. Crack Development and Failure Pattern. Figure 6 shows the destruction development process of specimen CW4X-D: $\theta = 0.05\%$ loading step, no crack appeared, and the average load at the corresponding loading step F equaled $11.2\%F_{max}$ (F_{max} is the average maximum load); when θ reached to 0.125%, vertical cracks were observed at the ends of the coupling beams, as shown in Figure 6(a), and the loading and unloading curves almost coincided, $F = 22.7\%F_{max}$; in

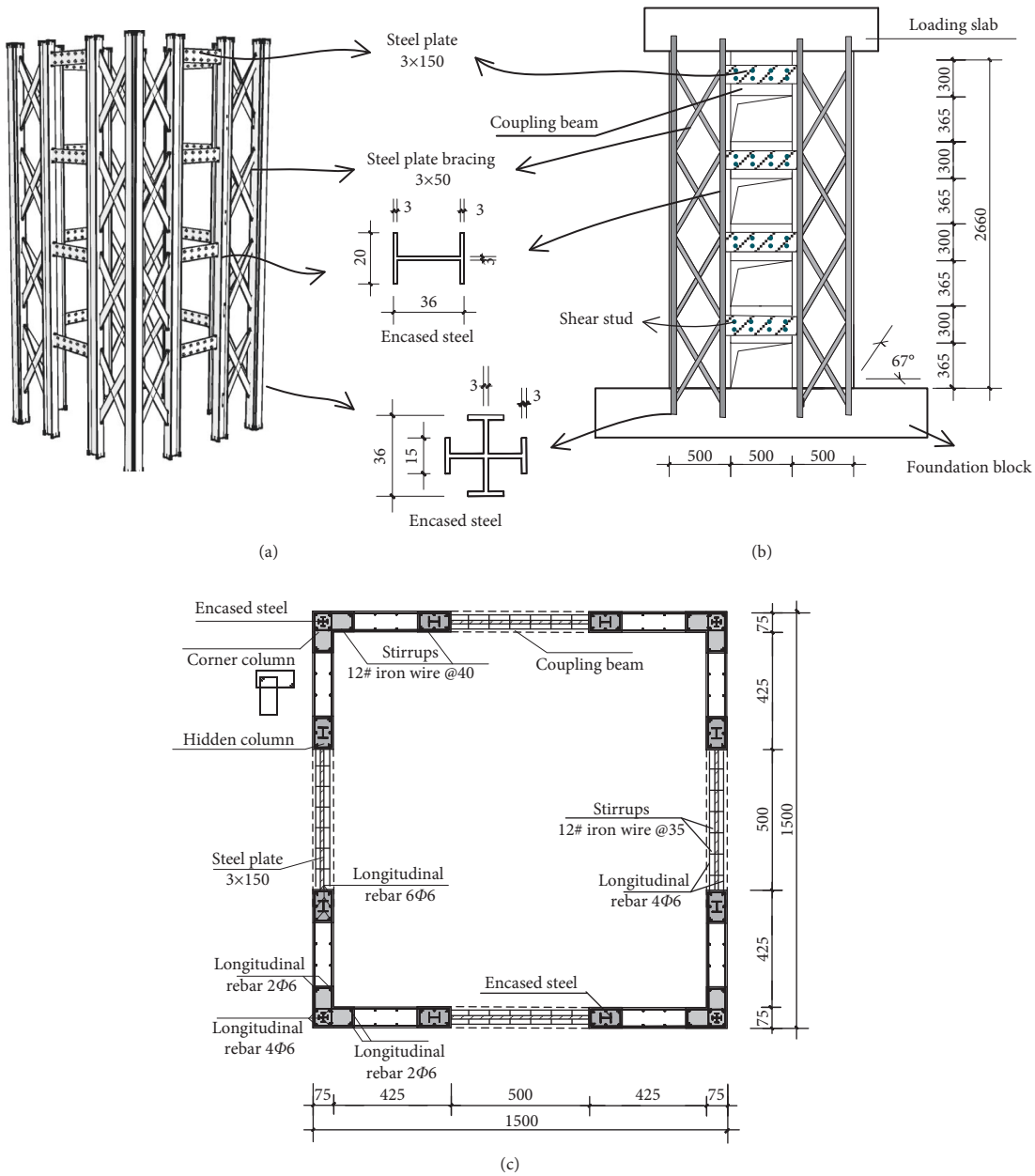

Figure 2: Details of steel-enhanced damping concrete core walls with concealed steel plate bracings (units: mm). (a) Inner frame. (b) Elevation. (c) Plan.

Table 1: Material strength of core wall specimens (unit: MPa).

Specimen	CW4X-1 [13]	CW4X-D
Concrete cubic compressive strength	33.5	38.1
Yield stress of reinforcement of flange/web	492.8	492.8
Yield stress of longitudinal reinforcement of edge members	407.0	407.0
Tensile strength of transverse wire of edge members	417.0	417.0
Yield stress of longitudinal reinforcement of coupling beam	407.0	407.0
Yield stress of transverse reinforcement of coupling beam	492.8	492.8
Yield stress of steel plate	269.0	269.0

$\theta = 0.25\%$ loading step, cracks appeared on wall limbs, where the oblique cracks were observed on the middle wall limbs, and horizontal cracks distributed on the end wall limbs, as shown in Figure 6(b), $F = 42.1\%F_{max}$; the middle wall limb cracks increased and extended to cross shapes, and the horizontal cracks on the end wall limbs propagated upward in the $\theta = 0.5\%$ loading step, shown in Figure 6(c), $F = 61.3\%$ F_{max}; $\theta = 0.75\%$, the cross cracks spread almost the entire

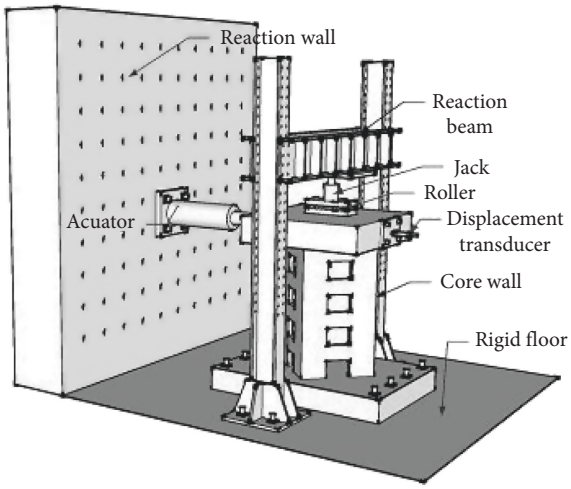

Figure 3: Test setup.

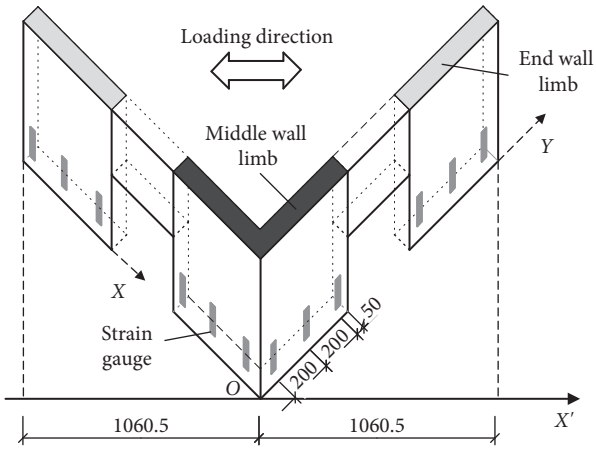

Figure 4: Strain gauge arrangement.

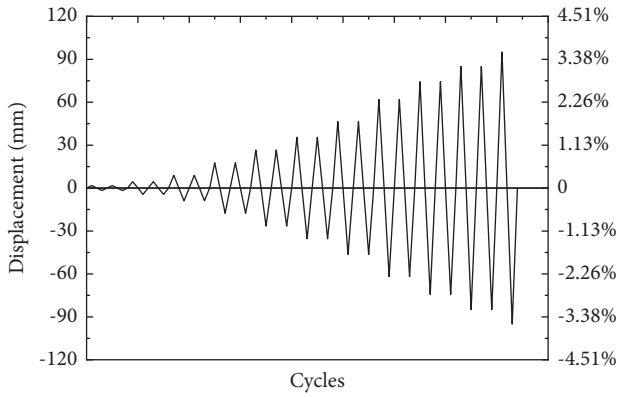

Figure 5: Loading protocol.

middle wall limbs, and the horizontal cracks on the end wall limbs expanded upwards and extended to the vicinity of the openings, shown in Figure 6(d), $F = 75.6\%F_{max}$; in the $\theta = 1\%$ loading step, cracks continued to increase, the horizontal cracks on the end wall limbs spread to the bottom of third floor coupling beams, and the oblique cracks on the middle wall limbs were fully developed, the crack distributions approached to the final failure pattern, as shown in Figure 6(e), residual deformation further increased in this loading step, and top drift ratio was slightly larger than the yield top drift ratio (the yield top drift ratio was 0.93%), $F = 88.2\%F_{max}$; in the $\theta = 1.32\%$ loading step, the end wall limb cracks continued to develop upwards, and oblique cracks appeared at the top of end wall limbs, and the longitudinal bars in the middle wall limbs yielded under compression in this loading step, and the residual deformation was further enlarged, shown in Figure 6(f), $F = 97.1\%$ F_{max}; $\theta = 1.69\%$, the specimen reached to the maximum strength; since this loading step till the end of test, the cracks scarcely increased, shown in Figure 6(g). Thereafter, the lateral loads decreased along with the increase of displacement; no obvious plastic hinge formed at the ends of coupling beams, while the concrete at the bottom of hidden columns and corner columns collapsed and the encased steel crushed, shown in Figures 6(h) and 6(i).

For better understanding of the influence of biaxial earthquake on the seismic performance to core wall, a comparison was made with the authors' [13] previously unidirectional tested core walls, as well the tests completed by Hou et al. [30]. Figures 7(a)~7(c) show the failure patterns of our former tested SEDCCW specimens of CW4X-1, CW3X-2, and CW4X-2 [13], for specimen CW4X-1, the coupling beams yielded and plastic hinges formed, which is a typical beam hinge mechanism, the webs had both horizontal cracks and oblique cracks, and the crack distributions and failure patterns of specimens CW3X-2 and CW4X-2 are similar with specimens CW4X-1. Figures 7(d)~7(e) are the failure pattern of diagonal test specimen CW-5, conducted by Hou et al. [30], as shown, the oblique cracks crossed and concentrated on the middle wall limbs ("Middle" for short), and the horizontal cracks distributed on the end wall limbs ("End" for short); the hidden columns and corner columns destroyed seriously. The coupling beams of specimen CW-5 crushed more seriously than the specimen CW4X-D, because specimen CW-5 had a beam span-depth ratio of 2.0, while the coupling beam span-depth ratio of specimen CW4X-D was 1.5. The coupling beam stiffness of specimen CW-5 was smaller than that of specimen CW4X-D. Hence, the coupling beams of specimen CW-5 yielded and could consequently participate in energy dissipating.

3.2. Force-Displacement Relationships. Figures 8 and 9 show the comparisons of hysteretic curves and skeleton curves for specimens CW4X-D and CW4X-1, respectively. As shown, the specimen CW4X-D performed plumper hysteretic curve than specimen CW4X-1.

3.3. Ductility, Stiffness, and Loading Capacity. The ductility coefficient μ is an important index which measures the structure seismic performance, given as

$$\mu_{\Delta} = \frac{\Delta_u}{\Delta_y}. \quad (1)$$

FIGURE 6: Destruction process of specimen CW4X-D. (a) $\theta = \pm 0.125\%$. (b) $\theta = \pm 0.25\%$. (c) $\theta = \pm 0.5\%$. (d) $\theta = \pm 0.75\%$. (e) $\theta = \pm 1\%$. (f) $\theta = \pm 1.32\%$. (g) $\theta = \pm 1.69\%$. (h) Final stage. (i) Failure pattern.

where Δ_u is the ultimate displacement, corresponding to 15% strength degradation of the maximum load; Δ_y is the yield displacement, calculated with the equivalent elastoplastic energy method [31]. The load-bearing capacities, deformation capacities, and ductility coefficients at key performance points for each specimen were shown in Table 2.

Inferred from Figures 8 and 9 and Table 2, it is found that, compared with specimen CW4X-1, specimen CW4X-D had lower initial stiffness and ductility coefficient, but higher bearing capacity, deformability, and yield displacement; the phenomena have come to the similar conclusions with Hou et al. [30]. The above results can be attributed to the fact that the diagonal test core wall had a lower stiffness anti-bending member than the unidirectional test core wall. The main anti-bending member for specimen CW4X-D was the end wall limb, and flange was the main anti-bending member for specimen CW4X-1, hence leading to a decrease in initial stiffness for the diagonal test core wall, but the internal forces were redistributed after the peak point, and all the middle wall limbs and end wall limbs participated in the bending moment resisting and energy dissipation, resulting in higher deformability for diagonal test specimen.

3.4. Energy Dissipation. The energy dissipation capacity of specimen was usually evaluated by using the cumulative energy dissipation, which can be expressed by the area enclosed by the hysteretic curves. The cumulative energy dissipation of specimens CW4X-D and CW4X-1 is shown in Figure 10.

Through comparison in Figure 10, it is indicated that specimen CW4X-1 consumed more energy in the early loading steps, but the energy dissipation of CW4X-D increased more rapidly with the loading step, when the lateral displacement reached to 75 mm ($\theta = 2.82\%$), specimen CW4X-D dissipated the same quantity of energy with specimen CW4X-1, and to the end of test, the cumulative dissipated energy of specimen CW4X-D was 441.14 kN·m, 45.7% higher than that of specimen CW4X-1. The phenomenon can be ascribed to the idea that the coupling beams of specimen CW4X-1 yielded before the peak point, and they were the main energy dissipating members, while for specimen CW4X-D, the coupling beams did not yield, thus in early loading steps, the energy could not be consumed so sufficiently as specimen CW4X-1. While after yield, all wall limbs of specimen CW4X-D crushed, they could actively

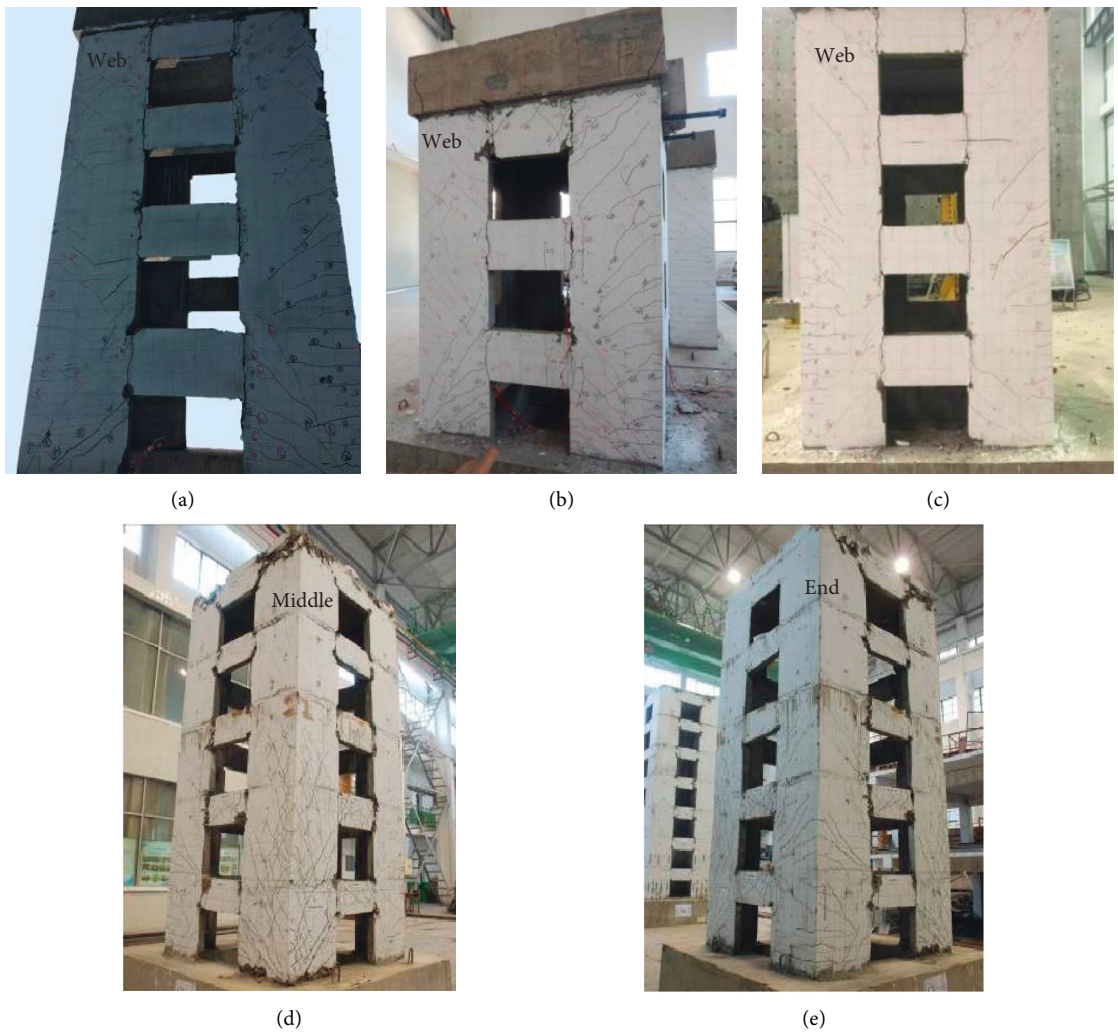

Figure 7: Failure patterns of available core walls. (a) CW4X-1 [13]. (b) CW3X-2 [13]. (c) CW4X-2 [13]. (d) CW-5 (middle) [30]. (e) CW-5 (end) [30].

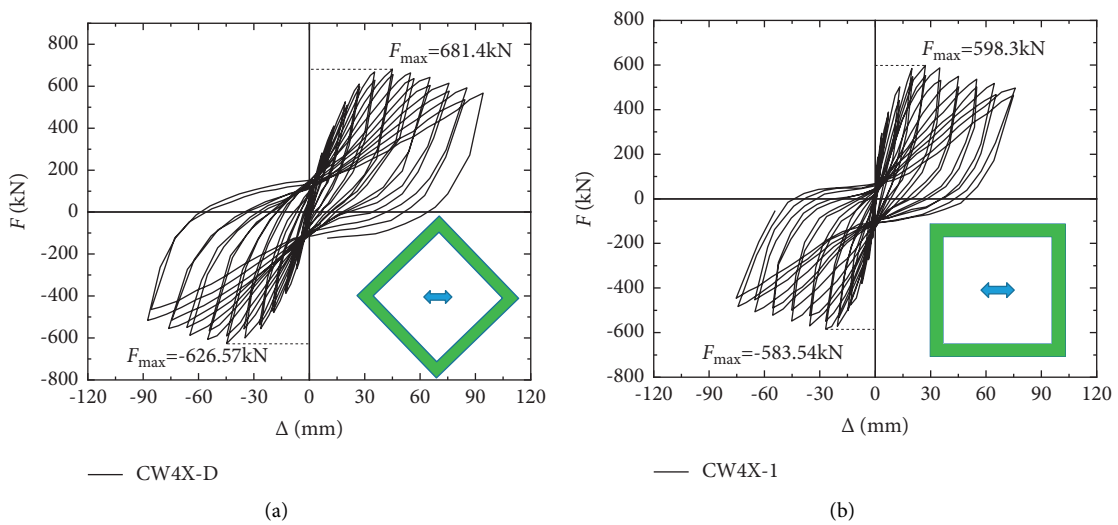

Figure 8: Hysteretic curves. (a) CW4X-D. (b) CW4X-1.

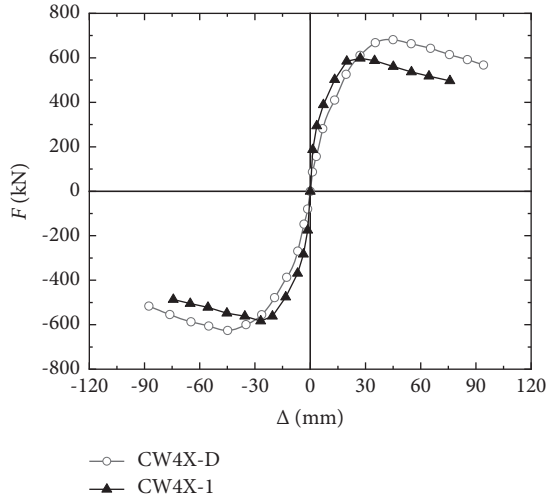

Figure 9: Skeleton curves.

Table 2: Load-bearing capacities and deformation capacities at key points and ductility coefficient.

Specimen	Loading direction	Initial cracking point		Yield point		Peak point		Ultimate point		μ_Δ
		F_{cr} (kN)	Δ_{cr} (mm)	F_y (kN)	Δ_y (mm)	F_{max} (kN)	Δ_{max} (mm)	F_u (kN)	Δ_u (mm)	
CW4X-D	Positive	156.2	3.29	582.3	24.54	681.4	45.07	579.1	89.94	3.66
	Negative	147.6	3.31	541.8	25.08	626.6	44.78	532.6	82.76	3.30
CW4X-1 [6]	Positive	223.5	3.59	521.3	14.78	598.3	27.23	508.5	69.27	4.69
	Negative	218.4	3.64	480.7	13.33	583.5	26.89	496.0	69.82	5.24

Table 3: Concrete parameters.

f_{cu} (MPa)	E_c (MPa)	ν	$f_{t,r}$ (MPa)	Dilation angel	Eccentricity	f_{b0}/f_{c0}	K	Viscosity parameter
35.1	3.1×10^4	0.2	2.61	30°	0.1	1.16	2/3	0.002

Note. f_{cu} denotes the cubic compressive of concrete, and E_c, f_{b0}, f_{c0}, and $f_{t,r}$ are the elastic modulus, uniaxial compressive strength, biaxial compressive strength, and uniaxial tensile strength of concrete, respectively; K is the constant stress ratio; ν is the poison's ratio.

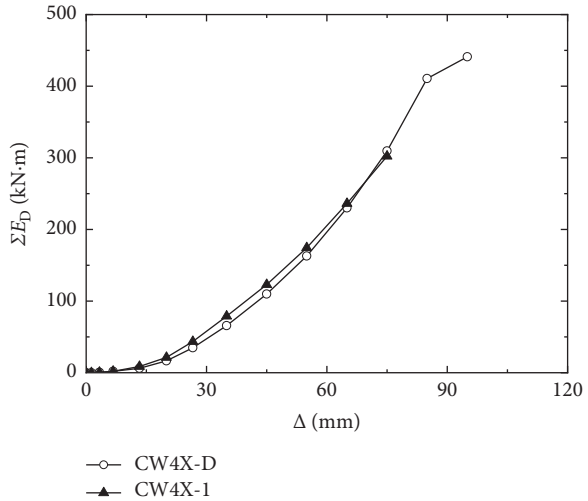

Figure 10: Cumulative energy dissipation.

participate in energy consuming, and more serious damage was consequently observed compared with specimen CW4X-1. The ultimate displacement and cumulative dissipated energy of specimen CW4X-D in any perpendicular direction (axis X and Y) can be calculated as equations (2) and (3), respectively. Accordingly, the ultimate displacement of specimen CW4X-D in one single direction was 12.2% lower than that of specimen CW4X-1, and the cumulative dissipated energy decreased by 27.1%.

$$\Delta_{u1} = \frac{\Delta_u}{\sqrt{2}}, \tag{2}$$

$$\Sigma E_{D1} = \frac{\Sigma E_D}{2}. \tag{3}$$

Δ_{u1} is the ultimate displacement in any perpendicular direction, ΣE_D is the total cumulative dissipated energy, and ΣE_{D1} is the cumulative dissipated energy in any perpendicular direction.

3.5. Strain Distribution. Core walls are spatially force members, in which the flanges resist most of the bending moments, and webs are the main shear resisting components thus endowing the core wall great stiffness and high bearing capacity. For H-shaped members, Box-shaped members, and T-shaped members, etc., shear flow develops where the

longitudinal strains in the center of the web and flanges lag behind the strains at the web-flange intersection of flanges; this phenomenon is named as the shear lag [32–34], shown in Figure 11. When subjected to oblique loads, the stress distributions changed, and thus it has quite different mechanical mechanisms; the measured concrete strain distribution of the specimen CW4X-D is shown in Figure 12.

From Figure 12, shear lag still existed in diagonal test core walls, while the strain distributions are varied from that of flanges. When subjected to positive lateral loads, the left end wall limb of specimen CW4X-D was in small eccentric tension (labeled as tension end wall limb), and the right end wall limb was in small eccentric compression (labeled as compression end wall limb), and vice versa. The above strain distributions can account for the crack distributions shown in Figure 6. The middle wall limbs bear most of the shear force; thus oblique cracks concentrated in the middle wall limbs. Compared with unidirectional test core wall, the coupling beam stiffness of diagonal test core wall was greater (in the loading direction, shown in Figure 4), the coupling beams rotated synchronously with the middle wall limbs and transferred the bending moments into axial forces, the axial forces were undertaken by end wall limbs, the working function of diagonal test core wall is similar to the frame-core wall (FCW), and the middle wall limbs of specimen CW4X-D can be corresponded to the core walls of FCWs, the coupling beams were similar to the outrigger truss of FCWs, and the end wall limbs were similar to the frames of FCWs, shown in Figure 13.

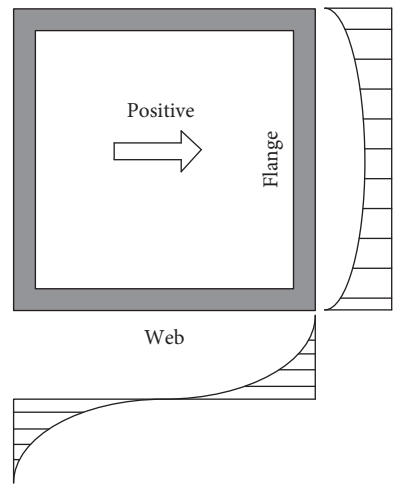

Figure 11: Shear lag.

4. Numerical Modeling

4.1. Model Information. To further study the mechanical mechanisms under biaxial earthquakes, a parametric analysis was conducted with ABAQUS on the basis of specimen CW4X-D in this section. The authors [35] found that the coupling beam span-depth ratio (l/h) and the axial compression ratio (n) were the main affecting factors on the shear lag and effective flange width of core walls, while diagonal test core walls had no obvious flange or web; the end wall limbs were in eccentric force states instead. Therefore, the influences of span-depth ratio and the axial compression ratio on the shear lag and the effective compression width of diagonal test core walls would be studied in this section.

The "C3D8R" element, "T3D2" element, and "S4R" element were used to simulate concrete, reinforcement, and steel, respectively. The reinforcement and steel were embedded in the "C3D8R" element; in this study, the "Standard" solution method was used. An uniform compressive stress was applied to the top of the loading plate to simulate axial compression, and then the horizontal load was applied.

4.2. Material Model

4.2.1. Concrete. The concrete damaged plasticity model was adopted in this article; the corresponding parameters are shown in Table 3.

4.2.2. Steel. The reinforcement, steel plate, and iron wire employed the elastic-plastic constitutive model in this study, the poison's ratio of them was taken as 0.3, the elastic modulus of iron wire and reinforcement was adopted as 2.05×10^5 MPa, and the elastic modulus of steel plate was 2.1×10^5 MPa; other mechanical indexes are shown in Table 1.

4.3. Analysis Model Verification. Figure 14 shows comparison between the test skeleton curves and simulated skeleton curves. The tensile damage nephograms of concrete for specimen CW4X-D and specimen CW4X-1 are shown in Figures 15(a) and 15(b), which can be compared with the crack distributions shown in Figures 6 and 7(a), respectively. Through the comparisons above, and the authors' former research [35], it can be indicated that the FEA models are able to predict the nonlinear responses of the SEDCCW well by using ABAQUS.

4.4. Parametric Analysis. Take the projection of the end wall limb on the Y' axis (Figure 16) as the abscissa and the compressive stress of the concrete as the ordinate values. The compressive stress distributions at different loading steps are shown in Figure 17(a). For comparison, the flange concrete stress of CW4X-1(FEA) [13, 35] is shown in Figure 17(b), in which the abscissa value is the distance from the web.

The wall limb concrete stress distributions of specimen CW4X-D (FEA) are significantly different from that of specimen CW4X-1 (FEA). The whole section of compression flange of specimen CW4X-1 (FEA) was under compression, while the compression end wall limb of CW4X-D (FEA) was under small eccentric compression, and some tensile stress was observed. The corner concrete stress of both specimens CW4X-D (FEA) and CW4X-1 (FEA) increased slowly after the top drift ratio reached to 0.5%, especially for the diagonal test core wall, the stress of which hardly increased with top drift ratio, and the compressive stress of corner concrete reached the maximum before the peak point.

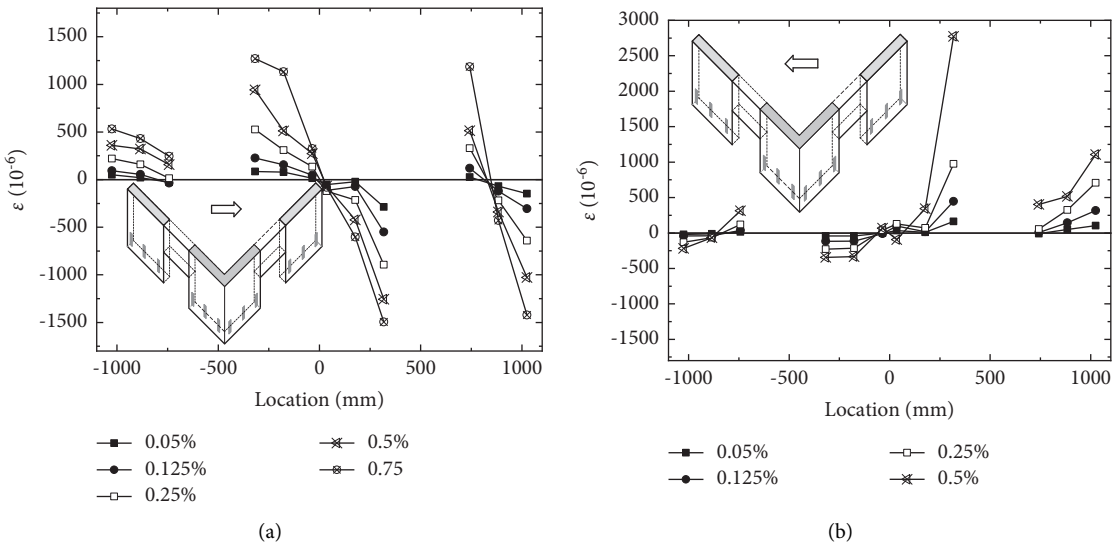

Figure 12: Wall limb strain distributions of CW4X-D. (a) Positive. (b) Negative.

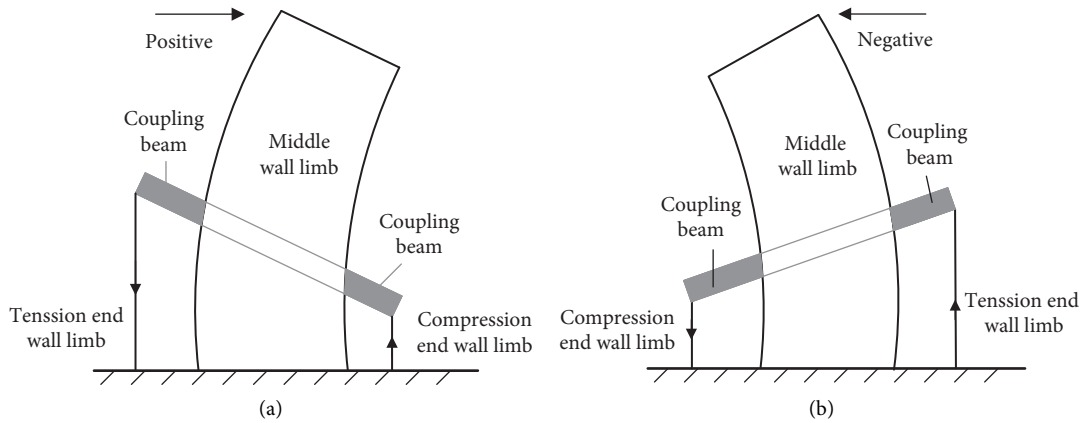

Figure 13: Simplified stress model of diagonal test core wall. (a) Positive. (b) Negative.

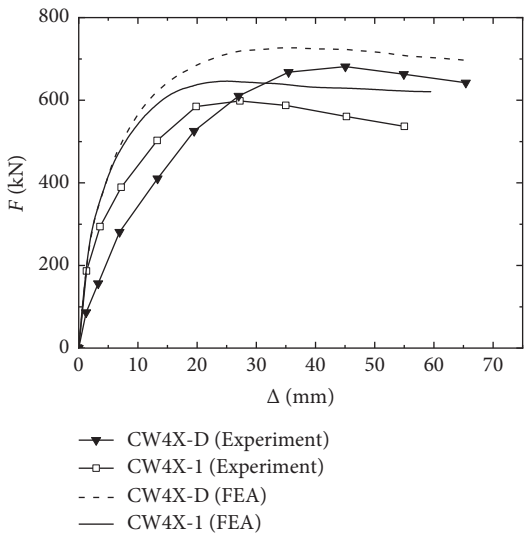

Figure 14: Comparison of hysteretic curves between experiment and FEA.

The shear lag effect is complicated, which brings inconvenience to the calculation of loading capacity for core walls, T-shaped beams, H-shaped beams, etc. Thus, the concept of effective width of flanges is always employed to simplify the calculation. However, the diagonal test core walls have no obvious flange, the end wall limbs of which take part in bending resisting instead of flanges. The effective flange width of unidirectional test core walls can be always calculated by (4), while for the diagonal test core walls, the concrete element arms of end wall limbs varied with location, the effective compression width of which can be calculated by (5).

$$b_e = \frac{\int_0^{b_f} \sigma \mathrm{d}z}{\sigma_0}, \tag{4}$$

$$b_e = \frac{\left(\int_0^{b_f} y\sigma \mathrm{d}z\right)}{(y_0\sigma_0)}. \tag{5}$$

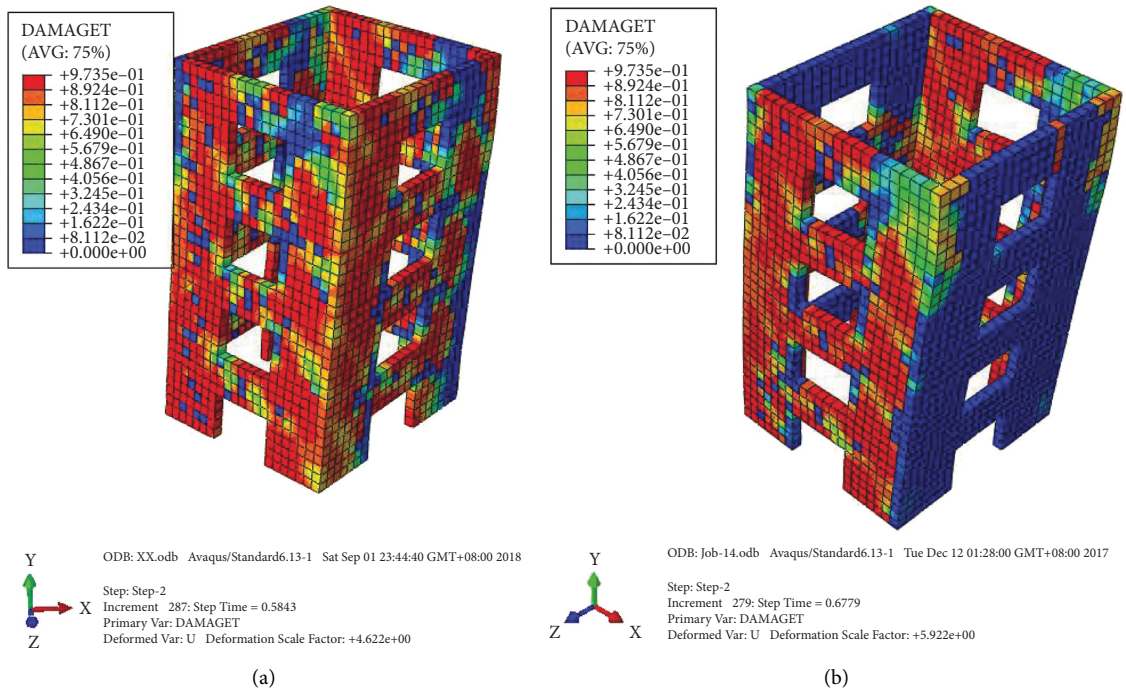

(a) (b)

Figure 15: Tensile damage nephogram of concrete for SEDCCWs (FEA). (a) CW4X-D. (b) CW4X-1.

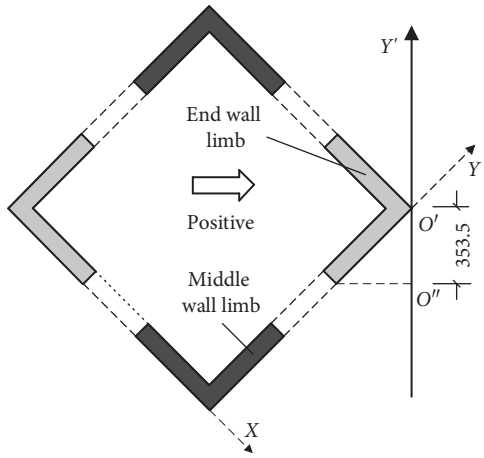

Figure 16: Coordinate system of end wall limb.

y is the arm of concrete element, which denotes the projected distance of concrete to point O'' on the axis Y', b_f is the projected length of end wall limb (353.5 mm, shown in Figure 16), y_0 denotes arm of corner concrete element, σ_0 presents the corner concrete stress, and Figure 18 shows the relation between top drift ratios and effective width of compression end wall limb (effective width for short).

From Figure 18, the effective width of specimen CW4X-D (FEA) decreased initially and then increased till the corner concrete element reached to the maximum stress, b_e reached to the minimum value meanwhile, and after that, the stress decreased again. The transformation law is almost the same as that of the effective flange width of unidirectional test core walls [35].

4.4.1. Coupling Beam Span-Depth Ratio. The coupling beams of specimen CW4X-D had almost the same function with the outrigger truss of FCW; the coupling beam stiffness significantly affects the shear lag of core wall. But it is still not sure about end wall limb stress distribution of core walls with varied values of l/h. Therefore, finite element analysis was conducted to investigate the stress distribution characteristics of the core walls with different coupling beam span-depth ratios, which varied from 1.5 to 1.25 and 2.5; the stress distributions at different top drift ratios are shown in Figures 17(a), 19(a), and 19(b), respectively. From comparison, the compression end wall limb of $l/h = 1.25$ core wall was almost full in compression, but the tensile stress was also observed in the compression end wall limbs of $l/h = 1.5$ and 2.5 core walls. Especially for the $l/h = 2.5$ core wall, the concrete stress of it was significantly lower than the other two core walls, and the maximum stress did not appear at the corner (point O). The above phenomena can be mainly attributed to the idea that the coupling beams functioned as the outrigger truss only if they had enough stiffness, while the stiffness of coupling beams reduced with the growth of l/h; hence it cannot make the compression wall limb under small eccentric compression.

Figure 20 shows the effective width of core walls with varied coupling beam span-depth ratios. The effective width of $l/h = 2.5$ core wall was even larger than b_f (353.6 mm), because the maximum stress was not in the corner. The minimum effective width $b_{e,\,\min}$ of each core wall is listed in Table 4, which indicates that the minimum effective width decreased with the coupling beam span-depth ratio.

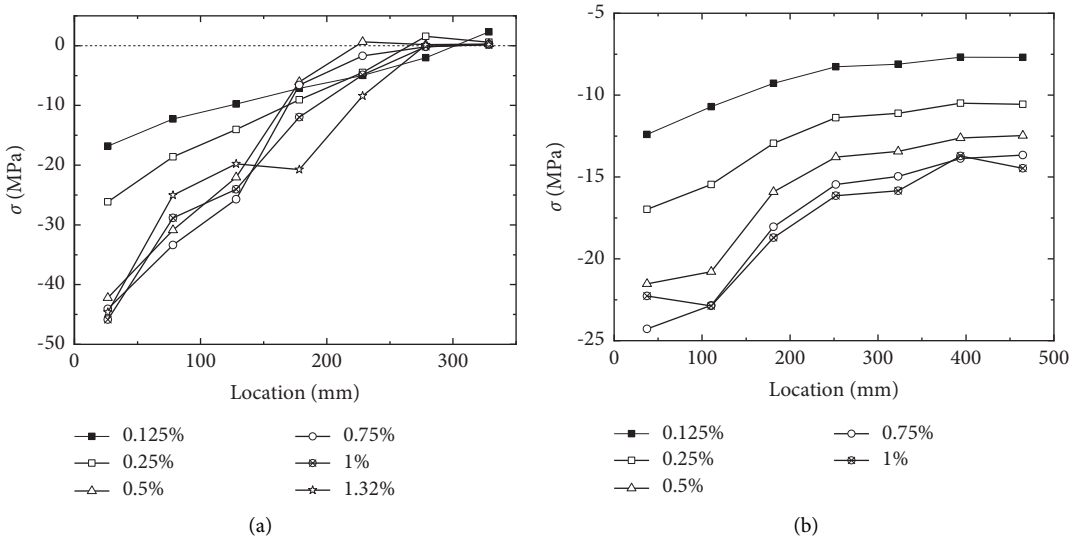

Figure 17: Concrete stress distributions at different loading steps (FEA). (a) CW4X-D($l/h = 1.5$, $n = 0.1$). (b) CW4X-1($l/h = 1.5$, $n = 0.1$) [31].

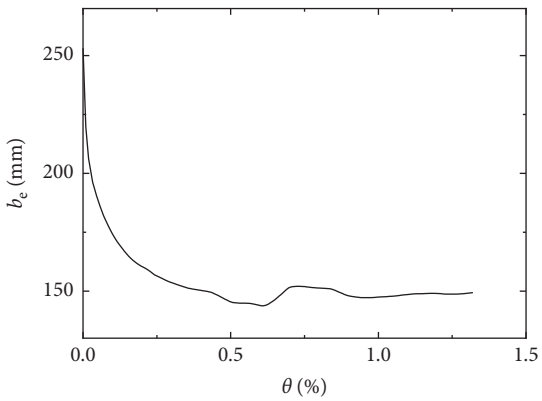

Figure 18: Effective width of specimen CW4X-D(FEA).

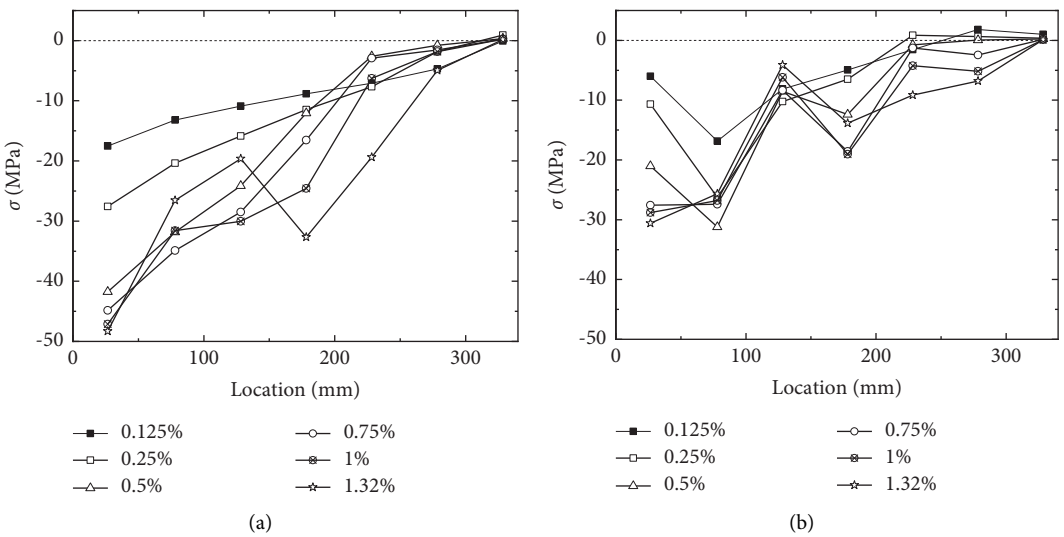

Figure 19: Concrete stress distributions of core walls with varied coupling beam span-depth ratios: (a) $l/h = 1.25$, $n = 0.1$. (b) $l/h = 2.5$, $n = 0.1$.

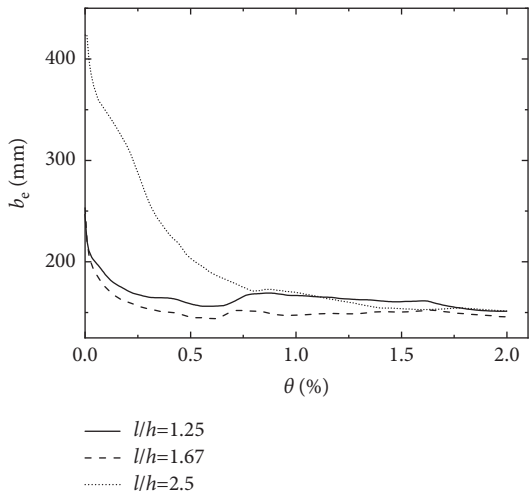

Figure 20: Effective width of core walls with varied span-depth ratios.

Table 4: Minimum effective width of core walls with varied span-depth ratios.

l/h	θ_0 (%)	$b_{e,\ \min}$ (mm)	η
1.25	0.573	156.1	0.442
1.67	0.948	154.57	0437
2.5	1.586	152.99	0.433

Note: θ_0 represents corresponding top drift ratio of the minimum effective width, $\eta = b_{e,\min}/b_f$.

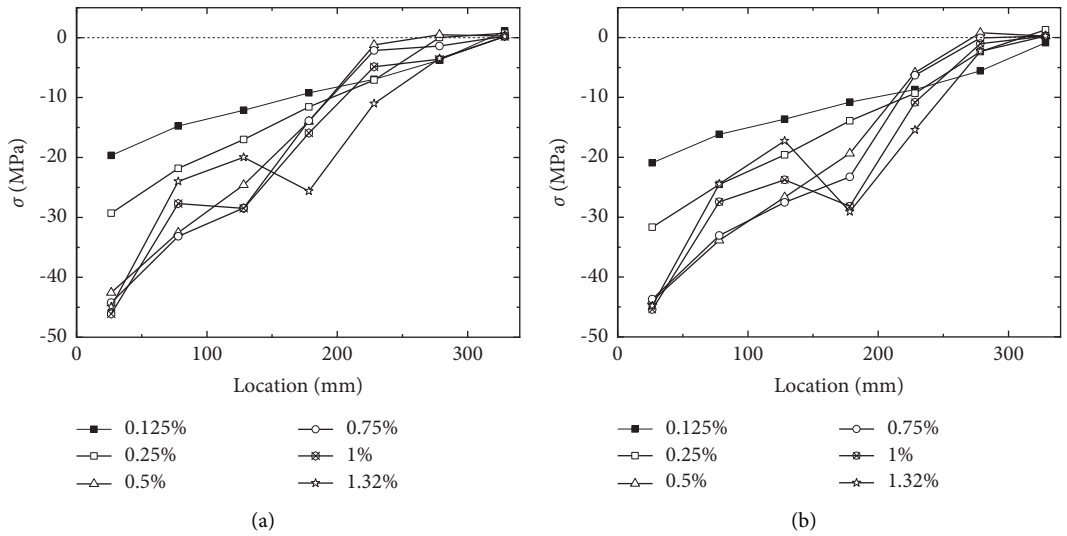

Figure 21: Concrete stress distributions of core walls with varied axial compression ratios. (a) $n = 0.2$, $l/h = 1.5$. (b) $n = 0.3$, $/h = 1.5$.

4.4.2. Axial Compression Ratio. The normal stress distributions and the effective width of the end wall limbs are shown in Figures 21 and 22, respectively; the axial compression ratio $n = 0.2$~0.3 (the FEA results for the core wall with the axial compression ratio of 0.1 is shown in Figure 17(a)). Table 5 lists the minimum effective width of each core wall ($b_{e,\min}$).

From Figures 21 and 22 and Table 5, the minimum effective width increased along with the axial compression ratio, but the end wall limb stress distribution was not well affected. The phenomenon is mainly because the normal stress distributed more uniformly with the increase of axial compression ratio, hence leading to the increase of the minimum effective width.

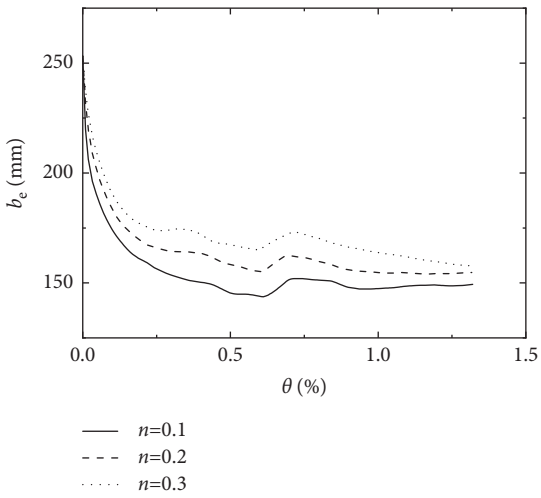

Figure 22: Effective width of core walls with varied axial compression ratios.

Table 5: Minimum effective width of core walls with axial compression ratios.

n	θ_0 (%)	$b_{e,\min}$ (mm)	η
0.1	0.948	154.57	0437
0.2	0.596	155.1	0.439
0.3	0.580	165.1	0.467

5. Conclusions

A diagonal loading test was conducted on one 1/6 scale steel-enhanced damping concrete core wall with steel plate bracings and compared with available core wall tests, then finite element analysis was carried out to study the mechanical mechanism and effective width of end wall limbs, and the following conclusions can be drawn:

(1) The diagonal test core walls exhibited quite different crack distributions and failure patterns from the unidirectional test core walls, in which the oblique cracks crossed and concentrated on the middle wall limbs, and the horizontal cracks were distributed on the end wall limbs. The hidden columns and corner columns were damaged more seriously compared with the unidirectional test core walls, but the coupling beam plastic hinge was not built. While for the unidirectional specimen, the coupling beams yielded and plastic hinges formed, both horizontal cracks and oblique cracks coexisted in the webs; the end wall limbs of core wall in this study were in small eccentric force states (small eccentric compression or small eccentric tension).

(2) Compared with unidirectional test core walls, the diagonal test core walls had lower initial stiffness and ductility coefficient but higher bearing capacity, deformability, and yield displacement, and more energy could be consumed.

(3) Shear lag also exists in diagonal test core walls, but diagonal test core walls have quite different mechanical mechanisms with the unidirectional test core walls, the end wall limb of which would be in small eccentric force states only if the core wall had a small coupling beam depth, while the axial compression ratio did not affect much the shear lag of diagonal test core walls; the effective compression width varied with loading steps, and the minimum value ($b_{e,\min}$) increased with the decrease of coupling beam depth, while $b_{e,\min}$ grow along with the axial compression ratio.

Data Availability

The data used to support the findings of this study are available from the corresponding author upon request.

Conflicts of Interest

The authors declare that they have no conflicts of interest.

Acknowledgments

This work was financially supported by National Natural Science Foundation of China (51578235), Hunan Natural Science Foundation (2020JJ5018 and 2020JJ5020), the Scientific Research Project of Education Department of Hunan Province (nos. 19A095, 19B099, 20B108, and 20C0363), and the Science and Technology Innovation Project of Yiyang City (2021YR02).

References

[1] W. L. Cao, M. Wang, and S. H. Wang, "Aseismic research of composite shear wall and core wall with rectangular concrete filled steel tube," *Engineering Mechanics*, vol. 25, no. S1, pp. 58–67, 2008, (in Chinese).

[2] H. Y. Dong, H. X. Geng, and J. W. Zhang, "Experimental study on seismic behavior of composite core walls with steel tube-reinforced concrete columns," *Journal of Beijing University of Technology*, vol. 37, no. 11, pp. 1720–1728, 2011, (in Chinese).

[3] W. L. Cao, X. M. Huang, Z. C. Lu, and X. Lu, "Experimental study on seismic behavior of reinforced concrete core walls with concealed bracings," *Earthquake Engineering and Engineering Vibration*, vol. 2, no. 3, pp. 81–86, 2005, (in Chinese).

[4] A. Rahai and F. Hatami, "Evaluation of composite shear wall behavior under cyclic loadings," *Journal of Constructional Steel Research*, vol. 65, no. 7, pp. 1528–1537, 2009.

[5] J. W. Zhang, H. X. Geng, W. L. Cao, and H. Y. Dong, "Seismic performance of composite core walls with steel tube-reinforced concrete columns and concealed steel truss," *Journal of Beijing University of Technology*, vol. 37, no. 11, pp. 1668–1676, 2011, (in Chinese).

[6] W. H. Chang, W. L. Cao, J. W. Zhang, and S. Zhao, "Study on seismic behavior of RC composite perforated core walls with concealed steel truss subjected to eccentric horizontal loading," *Earthquake Engineering and Engineering Vibration*, vol. 28, no. 2, pp. 77–84, 2008, (in Chinese).

[7] B. Wang, H. Jiang, and X. Lu, "Experimental and numerical investigations on seismic behavior of steel truss reinforced concrete core walls," *Engineering Structures*, vol. 140, pp. 164–176, 2017.

[8] W. G. Wong, P. Fang, and J. K. Pan, "Polymer effects on the vibration damping behavior of cement," *Journal of Materials in Civil Engineering*, vol. 15, no. 6, pp. 554–556, 2003.

[9] S. F. Nabavi, "Influence of polymers on concrete damping properties," in *Proceedings of the European Conference of Chemical Engineering Civil Engineering and Mechanical Engineering*, Tenerife Spain, November 2010.

[10] M. F. Wang and X. Y. Song, "Reinforcing admixtures and their effectiveness experiments for strength and damping of polymer modified concrete," *Advanced Materials Research*, vol. 168-170, pp. 1869–1874, 2010.

[11] M. F. Wang and X. Y. Song, "Experimental study on seismic performance of high damping concrete coupled shear wall with mixed concealed bracings and coupling beams with small span-depth ratios," *Earthquake Engineering and Engineering Dynamics*, vol. 33, no. 3, pp. 125–132, 2013, (in Chinese).

[12] M. F. Wang and Y. J. Wang, "Study on seismic performance of high damping concrete coupled shear walls with concealed steel plate bracings," *Engineering Mechanics*, vol. 34, no. 1, pp. 204–212, 2017, (in Chinese).

[13] M. f. Wang, D. Luo, and Z.-q. Hu, "Seismic performance of steel-enhanced damping concrete core walls with concealed steel plate bracings," *Engineering Structures*, vol. 213, pp. 110564–110623, 2020.

[14] M. F. Wang, Z. Q. Hu, and D. Luo, "Study on seismic performance of high damping concrete core walls with steel plate concealed bracings of different aspect ratio," *Earthquake Engineering and Engineering Dynamics*, vol. 38, no. 3, pp. 1–11, 2018, (in Chinese).

[15] W. Lam, R. K. Su, and H. Pam, "Experimental study on embedded steel plate composite coupling beams," *Journal of Structural Engineering*, vol. 131, no. 8, pp. 1294–1302, 2005.

[16] R. K. L. Su, W. Y. Lam, and H. J. Pam, "Experimental study of plate-reinforced composite deep coupling beams," *The Structural Design of Tall and Special Buildings*, vol. 18, no. 3, pp. 235–257, 2009.

[17] K. Beyer, A. Dazio, and M. J. N. Priestley, "Quasi-static cyclic tests of two U-shaped reinforced concrete walls," *Journal of Earthquake Engineering*, vol. 12, no. 7, pp. 1023–1053, 2008.

[18] R. Constantin and K. Beyer, "Behaviour of U-shaped RC walls under quasi-static cyclic diagonal loading," *Engineering Structures*, vol. 106, no. Jan.1, pp. 36–52, 2016.

[19] F. W. Qiu, W. F. Li, P. Pan, and J. R. Qian, "Quasi-static test research of reinforced concrete column under biaxial loading," *Journal of Building Structures*, vol. 22, no. 5, pp. 26–31, 2001, (in Chinese).

[20] F. Qiu, W. Li, P. Pan, and J. Qian, "Experimental tests on reinforced concrete columns under biaxial quasi-static loading," *Engineering Structures*, vol. 24, no. 4, pp. 419–428, 2002.

[21] H. Rodrigues, A. Arêde, H. Varum, and A. G. Costa, "Experimental evaluation of rectangular reinforced concrete column behaviour under biaxial cyclic loading," *Earthquake Engineering & Structural Dynamics*, vol. 42, no. 2, pp. 239–259, 2013.

[22] H. Bechtoula, S. Kono, and F. Watanabe, "Experimental and analytical investigations of seismic performance of cantilever reinforced concrete columns under varying transverse and axial loads," *Journal of Asian Architecture and Building Engineering*, vol. 4, no. 2, pp. 467–474, 2005.

[23] S.-Y. Chang, "Experimental studies of reinforced concrete bridge columns under axial load plus biaxial bending," *Journal of Structural Engineering*, vol. 136, no. 1, pp. 12–25, 2010.

[24] K. Song and Z. B. Li, "Tests on seismic behavior of RC short columns with high axial compression ratio under biaxial loading action," *Journal of Northeast Petroleum University*, vol. 38, no. 2, pp. 102–108, 2014, (in Chinese).

[25] A. Niroomandi, S. Pampanin, R. P. Dhakal, and M. S. R. Ashtiani, "Experimental study on the effects of bi-directional loading pattern on rectangular reinforced concrete walls," *Earthquake Engineering & Structural Dynamics*, vol. 50, no. 7, pp. 2010–2030, 2021.

[26] A. Habasaki, Y. Kitada, and T. Nishikawa, "Multi-directional loading test for RC seismic shear walls," in *Proceedings of the 12th World Conference on Earthquake Engineering*, pp. 1–8, The New Zealand Society for Earthquake Engineering, Auckland, New Zealand, February 2000.

[27] T. Hiroshi, K. Yoshio, and N. Takao, "Multi-axis loading test on RC shear walls overview and outline of two directional horizontal loading test," in *Proceedings of the Transactions of the 16th International Conference on Structural Mechanics in Reactor Technology*, pp. 1–8, International Association for Structural Mechanics in Reactor Technology, Washington DC, August 2001.

[28] H. Torita, R. Matsumoto, and Y. Kitada, "Shaking table test of RC box-type shear wall in multi-axes loading," in *Proceedings of the 13th World Conference on Earthquake Engineering*, World Conference on Earthquake Engineering, Vancouver, August 2004.

[29] X. L. Du, P. Jia, and J. Zhao, "Seismic behavior of reinforced concrete core walls under biaxial cyclic lateral loading," *Journal of Building Structures*, vol. 33, no. 10, pp. 47–52, 2012, (in Chinese).

[30] W. Hou, Q. X. Shi, and Y. Liu, "Experimental study on seismic behavior of reinforced concrete core walls under diagonal low cyclic loading," *Farmaco*, vol. 30, no. 12, pp. 213–227, 2013, (in Chinese).

[31] T. Paulay and M. J. N. Priestley, *Seismic Design of Reinforced concrete and Masonry Buildings*, John Wiley & Sons, New York, 1992.

[32] R. D. Hoult, "Shear lag effects in reinforced concrete C-shaped walls," *Journal of Structural Engineering*, vol. 145, no. 3, Article ID 04018270, 2019.

[33] A. K. H. Kwan, "Shear lag in shear/core walls," *Journal of Structural Engineering*, vol. 122, no. 9, pp. 1097–1104, 1996.

[34] S. J. Zhou, "Finite beam element considering shear-lag effect in box girder," *Journal of Engineering Mechanics*, vol. 136, no. 9, pp. 1115–1122, 2010.

[35] Z. Q. Hu and M. F. Wang, "Analysis on effective flange width of concrete core walls with steel plate concealed bracings," *Journal of Hunan University*, vol. 46, no. 3, pp. 50–58, 2019, (in Chinese).